This is a copy of the published version, or version of record, available on the publisher's website. This version does not track changes, errata, or withdrawals on the publisher's site.

# Microscopic diffusion in cationic vesicles across different phases

Jyoti Gupta, V. K. Sharma, H. Srinivasan, Himal Bhatt, S. Kumar, M. Sarter, V. García Sakai, and S. Mitra

**Published version information**

**Citation:** J Gupta et al. Microscopic diffusion in cationic vesicles across different phases. Phys Rev Materials 6, no. 7 (2022): 075602

**DOI:** 10.1103/PhysRevMaterials.6.075602

This version is made available in accordance with publisher policies. Please cite only the published version using the reference above. This is the citation assigned by the publisher at the time of issuing the APV. Please check the publisher's website for any updates.

This item was retrieved from **ePubs**, the Open Access archive of the Science and Technology Facilities Council, UK. Please contact epublications@stfc.ac.uk or go to http://epubs.stfc.ac.uk/ for further information and policies.

# Microscopic diffusion in cationic vesicles across different phases

Jyoti Gupta,[1,3] V. K. Sharma,[1,3,*] H. Srinivasan,[1,3] Himal Bhatt,[2,3] S. Kumar,[1] M. Sarter,[4] V. García Sakai,[4] and S. Mitra[1,3]

[1]*Solid State Physics Division, Bhabha Atomic Research Centre, Mumbai 400085, India*
[2]*High Pressure & Synchrotron Radiation Physics Division, Bhabha Atomic Research Centre, Mumbai 400085, India*
[3]*Homi Bhabha National Institute, Mumbai 400094, India*
[4]*ISIS Neutron and Muon Source, Science and Technology Facilities Council, Rutherford Appleton Laboratory, Didcot OX11 0QX, United Kingdom*

(Received 7 January 2022; accepted 24 June 2022; published 12 July 2022)

Understanding the phase behavior and microscopic diffusion mechanism of cationic vesicles is crucial for controlled-release kinetics in gene/DNA transfection. Here, we report our findings on the structure, phase behavior, and microscopic dynamics of a vesicle based on a cationic double-chained surfactant, dihexadecyldimethylammonium bromide (DHDAB), which is a promising candidate for a nonviral gene/DNA carrier. Small-angle neutron-scattering measurements reveal that DHDAB aggregates are in the form of unilamellar vesicles. Calorimetric studies show a strong thermal hysteresis in the heating and cooling cycles following different pathways. Two first-order transitions are observed at 303 and 318 K in the heating cycle. Fourier transform infrared spectroscopy reveals that the first transition (at 303 K) is associated with a polymorphic (solid-solid) transition from coagel to an intermediate crystalline (IC) phase, and subsequently the second transition (at 318 K) is an order-disorder transition from IC to the fluid phase. Interestingly, it is found that in the cooling cycle, the fluid phase directly transforms back into the coagel phase without passing through the IC phase. This is also confirmed by an elastic fixed window scan (EFWS) using incoherent neutron scattering. The phase behavior of DHDAB is in strong contrast to that of its longer-chain counterpart, dioctadecyldimethylammonium bromide (DODAB), where the intermediate gel phase was observed during the cooling cycle. Moreover, no polymorphic transition was observed in the heating cycle of DODAB, in which the coagel phase directly converts to the fluid phase. These sharply contrasting phase behaviors for DHDAB and DODAB suggest the strong dependence of membrane phase behavior to the alkyl chain length. EFWS measurements reveal that the phase transitions observed in the DHDAB membrane are associated with strong changes in the DHDAB dynamics. The changes in conformational entropy of DHDAB molecules estimated from EFWS confirm that the coagel-fluid and IC-fluid phase transitions are accompanied by strong changes in the conformations of the alkyl chains. The microscopic dynamics of DHDAB molecules in each of these phases is investigated by employing quasielastic neutron-scattering (QENS). In the ordered phases (coagel and IC), only localized internal dynamics of the DHDAB is observed in the QENS spectra. However, in the fluid phase, the presence of a long-range lateral diffusion is detected in addition to the localized internal dynamics of the alkyl chain. The lateral motion is found to follow Fickian diffusion. The internal dynamics of DHDAB depends on the phase state of the bilayer. In the ordered phase, the internal dynamics is described by a fractional uniaxial rotational diffusion model. However, in the fluid phase, where alkyl tails are disordered with significant gauche defects, the internal dynamics is described using localized translation within confined spheres. This study highlights the rich phase behavior of the DHDAB membrane and the surfactant dynamics across these phases.

DOI: 10.1103/PhysRevMaterials.6.075602

## I. INTRODUCTION

Gene therapy has become one of the most prominent approaches to the treatment of hereditary diseases [1–4]. The transfer of a gene/DNA to the nucleus of a target cell is challenging as it requires vector/DNA complexes to cross a number of barriers [4]. The vector needs to release the DNA inside the cell, which must pass the nuclear membrane before transgene expression, as well as to protect the plasmid from extracellular environments [5]. Nonviral vectors [4,6–8] are emerging as favorable alternatives to viral vectors for DNA transfection, which suffer from problems such as immunogenicity, toxicity, and practical issues in large production and quality control. Due to the ease of synthesis and tailoring, cationic surfactants are currently the most widely employed constituents of nonviral gene carriers [7,9,10]. Despite synthesis of a large number of double-chained cationic surfactants, the correlation between the cationic amphiphilic chemistry and transfection efficacy has not yet been established due to the complexity of the pathways of transfection. Hence, the optimization of the molecular structure of the cationic surfactant is still largely empirical. However, it has been shown that transfection activity depends in a systematic way on the surfactant hydrocarbon chain structure [11].

*sharmavk@barc.gov.in

 ©2022 American Physical Society

Surfactant molecules are amphiphilic in character and self-assemble in aqueous medium to form different types of structures (e.g., micelles, vesicles, etc.) under favorable conditions. These vesicle bilayer structures offer unique opportunities to mimic complex cell membranes and to develop nonviral gene carriers. Vesicle bilayers show rich phase behavior with amphiphilic molecules arranged in the different phases such as crystalline, gel, fluid, depending on parameters such as temperature, hydration, pH, molecular architecture, and concentration [12]. The crystalline phase (e.g., coagel, subgel) has the highest order among the lamellar phases, whereas the fluid phase is highly disordered and has a large area per surfactant. The physics of the rich phase behavior and the associated transitions are thus scientifically interesting and of high biological relevance. Various experimental methods such as differential scanning calorimetry (DSC) [13,14], Fourier transform infrared spectroscopy (FTIR) [15–17], diffraction [18,19] and neutron elastic intensity scans [13,20–22] have been widely employed to investigate the phase behavior of the model membrane systems. These methods are highly complementary to each other and provide microscopic insights on the phase behavior. DSC measures changes in the enthalpy of the system during the phase transition; IR-active bands originating from the fundamental vibrations involving $CH_2$ group (i.e., C-H stretching, $CH_2$ scissoring modes, etc.) which strongly depend on the *trans-gauche* ratio, are ideal for identifying the main phase transition of the membranes. This is possible as the main phase transition is associated with alkyl tails which essentially transform themselves from all *trans* state to a disordered state with significant *gauche* defects (i.e., conformational disorder). Hence, FTIR measurements provide information on the structure of surfactant molecules during the phase transition that can be used to supplement the DSC results. Neutron elastic intensity scans provide information about whether phase transitions are accompanied with sharp changes in the membrane dynamics. Hence, by combining these methods one can get microscopic insights on the phase behavior in the model membrane systems.

Dialkyldimethylammonium bromides, $(C_nH_{2n+1})_2(CH_3)_2N^+Br^-$, are a family of double-chain cationic surfactants with a positively charged dimethylammonium head group and varying chain lengths ($n = 12, 14, 16, 18$) [23,24], and are promising candidates for nonviral gene carriers. They have also been found as useful surfactant-based model membrane systems which mimic biological processes like endocytosis [25,26]. In aqueous solution, these surfactants show a rich phase behavior that strongly depends on the alkyl chain length. The transition temperature varies nonlinearly with increasing chain length [23]. In the series of these surfactants, dioctadecyldimethylammonium bromide (DODAB; $n = 18$) has been the most widely studied, owing to its widespread applications [13,20,27–31]. At low temperatures, DODAB bilayers can be in coagel or gel phases depending on the concentration [13,20,29,31,32]. In both phases, the alkyl chains are ordered and in an almost all *trans* configuration, with differences in head group area, packing density, hydration, and dynamics. As the temperature increases, they undergo the main phase transition and form the fluid phase, in which surfactant molecules are highly disordered with the significant gauche defects in the alkyl chains. Its closest neighbor dihexadecyldimethylammonium bromide (DHDAB; $n = 16$), despite showing promising applicability, has been studied very scarcely. The molecular structure of both surfactants is shown in Fig. 1. At a lower concentration (∼2 mM) and low temperature, DHDAB forms a bilayer structure in gel phase [24]. With increasing temperature, DHDAB bilayer goes to a liquid crystalline phase via a main phase transition at 301 K [24]. At a concentration of 5 mM, DHDAB bilayer goes through an additional transition at 315 K, which is called post-transition and corresponds to morphological changes in the liposome [23]. At 303 K, DHDAB aggregates form polydisperse spherical vesicles and are found to be in single phase in the concentration range of 1.5 to 80 mM [33]. However, above 80 mM, vesicles coexist with an additional lamellar phase. Addition of different additives is found to alter the structure and phase behavior of the DHDAB membrane [34–41]. Though the structure of the DHDAB bilayer in the absence and presence of additives has been studied in detail, there is not much information available on the dynamics of cationic DHDAB membrane. The dynamical behavior of the surfactants plays an important role in controlling the various physiological processes and release kinetics of the DNA encapsulated in the nonviral carriers.

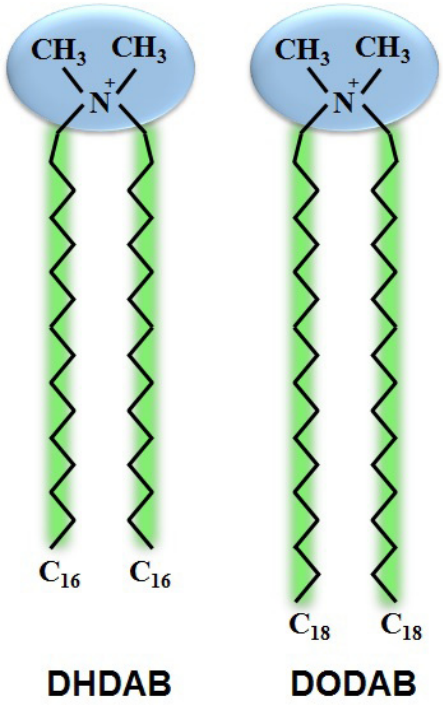


FIG. 1. Molecular structures of DHDAB and DODAB which have same positively charged quaternary ammonium head group but differ in the alkyl chain lengths. DHDAB has two alkyl chains, each with 16 carbon atoms whereas DODAB has two alkyl chains, each with 18 carbon atoms.

The dynamics of a membrane is fairly complex, encompassing multiple relaxation processes at the local and global scales. It covers a wide range of timescales from a few femtoseconds (molecular vibration) to minutes (flip-flop). The dynamics of a membrane determines the viscoelastic properties of the bilayer which play a vital role in the release kinetic of DNA/gene transfection. Membrane dynamics

can be studied using various experimental methods including nuclear magnetic resonance (NMR) [42,43], fluorescence spectroscopy [28,44], electron paramagnetic resonance [45], quasielastic neutron scattering (QENS) [46–53], and computational methods like molecular dynamics simulation [54,55]. In this work, we choose QENS as it is ideal to study membrane dynamics in the timescale of subpicoseconds to nanoseconds and in the length scale of few angstroms. This technique has been widely employed to investigate dynamical landscape in membranes [13,20–22,27–29,31,46–50,56]. All important information pertaining to timescale, geometry, and potential energy of the dynamics can be obtained using QENS technique.

Bilayer membrane phase transitions are typically accompanied by sharp changes in the membrane dynamics. This has been characterized by a recent study based on the flexible strings model [57] used to explore the phase transitions in the dipalmitoylphosphatidylcholine (DPPC) lipid membranes; a sharp increase in lateral diffusivity across the main bilayer phase transition is the result of the combined effect of a change in entropic repulsive forces and area per lipid. This model can be extended to the surfactant-based membranes investigated in this study, taking into account differences in intermolecular interactions. Unlike DPPC, these surfactants have a much smaller and strongly polar cationic head group. This leads to a very asymmetric interaction potential along the bilayer normal, where there is a strong electrostatic repulsion between the head groups and a relatively weak van der Waals interaction in the tail region. This fundamental difference in the molecular interaction between DPPC and DHDAB/DODAB surfactant manifests in the starkly different phase behavior observed. The surfactant membranes exhibit exotic phase behavior which depends on thermal history [13], which has been rationalized through a nonsynchronous ordering in the case of DODAB membranes.

Here, we report a detailed study of structural, dynamical, and phase behaviors of the DHDAB bilayer as studied using small-angle neutron scattering (SANS), dynamic light scattering (DLS), DSC, FTIR, elastic incoherent neutron scattering [known as elastic fixed window scan (EFWS)], and QENS. Observed results are compared with the DODAB bilayer which has the same head group but a longer alkyl chain. Comparison of these two bilayer systems provides a comprehensive understanding of dynamical and phase behavior of these cationic surfactants.

## II. MATERIALS AND METHODS

### A. Materials and sample preparation

DHDAB, powder (>97%) and DODAB, powder (>98%) were procured from Tokyo Chemical Industries Co. Ltd. $D_2O$ (99.9%) was purchased from Sigma-Aldrich; 70 mM DHDAB and DODAB vesicles were prepared by mixing appropriate amounts of surfactant in $D_2O$. The obtained mixture was kept under magnetic stirring for ∼1 h at 340 K. A concentration of 70 mM was chosen to compare results with the earlier study on DODAB with the same concentration [13]. For all the measurements including DLS, DSC, and FTIR, samples were prepared in $D_2O$.

### B. DLS measurements

To characterize the size distribution of the aggregates, DLS measurements were carried out using a Malvern Zetasizer Nano ZS (He−Ne laser wavelength, $\lambda = 633$ nm at 30 mW laser power, at a backscattering setup angle of $\theta = 173^\circ$). Samples for DLS were diluted to 1% of the 70 mM DHDAB and were filled in disposable sizing cuvettes. DLS measurements were carried out at three temperatures, namely 300, 315, and 330 K. Samples were thermally equilibrated for 5 min before each measurement.

### C. SANS measurements

To investigate the structure of the aggregates, SANS measurements were performed on 70 mM DHDAB at 300, 315, and 330 K using the SANS diffractometer at Guide Tube Laboratory, Dhruva Reactor, Bhabha Atomic Research Centre, Mumbai, India [58]. A monochromatic beam of neutrons was made incident on the samples and scattered neutrons were collected using one-dimensional $He^3$ position-sensitive detector in a wave-vector transfer $Q(= 4\pi \sin\theta/\lambda$, where $\lambda = 5.2$ Å is the wavelength of the incident neutrons and $2\theta$ is the scattering angle) range about 0.01–0.3 $Å^{-1}$. Data were corrected for background, empty cell, and solvent contributions and normalized to absolute units of cross section using standard protocols.

### D. DSC measurements

DSC thermograms were recorded on 70 mM DHDAB from 280 to 335 K using DSC 1 start system by Metter Toledo Instrument. The scan rate of the measurement was kept 5 K/min. To investigate hysteresis and reversibility of the transitions, measurements were carried out in heating as well as in cooling cycles.

### E. FTIR measurements

Infrared spectroscopic studies were carried out on 70 mM DHDAB using Bruker IFS125 HR Fourier transform spectrometer employing liquid-nitrogen cooled HgCdTe detector, KBr beamsplitter, and globar source. For *in situ* variable-temperature conditions, a heatable sample stage with a temperature resolution of 1 K was mounted on the sample stage of the spectrometer. The sample chamber for the liquid specimens was constructed using two IR transparent $CaF_2$ windows, with a path length of ∼60 $\mu$m. The data were measured in transmission mode in the 900–4000 $cm^{-1}$ spectral range at various temperatures from room temperature to 324 K. A total of 120 scans were co-added in all the measurements. For background correction, the data were recorded using an empty sample chamber with zero path length. The spectra were fitted using a Gaussian line shape.

### F. EFWS and QENS measurements

EFWS and QENS measurements were carried out on 70 mM DHDAB vesicles using the high-resolution backscattering spectrometer, IRIS, at the ISIS Pulsed Neutron and Muon Source (Rutherford Appleton Laboratory, UK) [59]. The spectrometer was used with its pyrolytic graphite (002) analyzer which offers an energy resolution of ∼17.5 $\mu$eV. Experiments

were carried out in the energy-offset mode which provides an energy transfer range of −0.3 to +1.0 meV. The available wave-vector transfer ($Q$) range in this configuration was 0.6–1.8 Å$^{-1}$. EFWS measurements for DHDAB were carried out in the temperature range of 285–333 K in both heating and cooling cycles. EFWS measurements showed a large hysteresis in the phase behavior of the membrane. For direct comparison, EFWS measurements were also performed on 70 mM DODAB using the identical configuration of the spectrometer. QENS experiments were carried out on DHDAB vesicles on selected temperatures as determined by the EFWS measurements, namely 300, 315, and 330 K in the heating cycle, and 315 and 300 K, in the cooling cycle. To estimate the solvent contribution, QENS experiments were also carried out on pure $D_2O$ at the same temperatures. Annular aluminum sample cells with an internal spacing of 0.5 mm were used for the neutron-scattering measurements to ensure no more than 10% scattering and minimize multiple-scattering effects. To obtain the instrument resolution, a QENS measurement was also carried out on standard vanadium. Standard data corrections were carried out using the MANTID software [60].

## III. DATA ANALYSIS

### A. DLS

The intensity autocorrelation function, $g^2(\tau)$, is related to the first-order autocorrelation function of the electric field, $g^1(\tau)$, by the Siegert relation:

$$g^2(\tau) = C[g^1(\tau)]^2 + 1, \tag{1}$$

where $C$ is the spatial coherence factor which depends mainly on the instrument optics and $\tau$ is the correlation decay time. For a monodisperse vesicle system, an ideal case, $g^1(\tau)$ should decay as a single exponential. However, in a real situation, there is a polydispersity in the size of the aggregates and for such system $g^1(\tau)$ can be written as

$$g^1(\tau) = \int_0^\infty G(\Gamma_{\mathrm{DLS}}) \exp(-\Gamma_{\mathrm{DLS}}\tau) d\Gamma_{\mathrm{DLS}},$$

where $G$ ($\Gamma_{\mathrm{DLS}}$) represents the relative weight factor for relaxation rate $\Gamma_{\mathrm{DLS}}$. For narrow polydispersity, the above expression can be simplified to the well-known cumulant expansion [61]

$$g^1(\tau) = \exp\left[-\overline{\Gamma_{\mathrm{DLS}}}\tau + \frac{\mu_2\tau^2}{2}\right], \tag{2}$$

where first and second cumulant, $\overline{\Gamma_{\mathrm{DLS}}}$and $\mu_2$, are the mean decay constant and variance, respectively. The ratio of the variance to the square of the mean is a measure of the polydispersity in the diffusion coefficient or hydrodynamic size and represented by the polydispersity index (PI).

Cumulant analysis for a polydisperse system requires that $\mu_2\tau^2 \ll 1$. However, for a system having large PI, at large $\tau$ values, $\mu_2\tau^2$ becomes comparable to 1, which leads a deviation from the expected decay of correlation function especially at large $\tau$ values. For such cases, CONTIN [62] analysis is widely used, which employs inversion of the Laplace integral equation that provides full distribution in the size.

### B. SANS

In SANS, one measures the scattering intensity as a function of $Q$, which is related to differential scattering cross section per unit volume ($d\Sigma/d\Omega$). For a system of monodisperse interacting particles in a medium, $d\Sigma/d\Omega$ can be expressed as [63,64]

$$\left(\frac{d\Sigma}{d\Omega}\right)(Q) = nP(Q)S(Q) + B, \tag{3}$$

where $n$ denotes the number density of particles, $P(Q)$ is the intraparticle structure factor, and $S(Q)$ is the interparticle structure factor. $B$ is a constant term representing the incoherent background, which is mainly due to the hydrogen present in the sample.

The intraparticle structure factor is the square of the form factor and provides information of the geometrical parameters such as shape, size, and size distribution, etc. of the scatterers. For vesicles having inner radius $R$ and thickness $dR$, the form factor $P(Q)$ can be expressed as [64]

$$P(Q) = 16\pi^2(\rho_c - \rho_s)^2 \times\left[(R+dR)^3\frac{\sin Q(R+dR) - Q(R+dR)\cos Q(R+dR)}{Q^3(R+dR)^3} - R^3\frac{\sin QR - QR\cos QR}{Q^3R^3}\right]^2, \tag{4}$$

where $\rho_c$ and $\rho_s$ are the scattering length densities of the scatterer and solvent, respectively.

The $S(Q)$, on the other hand, is determined by the interparticle correlations and hence provides information about the interactions present among the scatterers. However, for a sufficiently dilute system, S($Q$) can be approximated to unity. The measured SANS data have been analyzed by comparing the scattering from different models to the experimental data. Throughout the data analysis, corrections were made for instrumental smearing, by smearing the scattered profiles with the appropriate resolution function, before comparing with the measured data. The fitted parameters in the analysis were optimized using a nonlinear least-square fitting program [64,65].

### C. QENS

In a QENS experiment, the scattering signal is measured as a function of the energy transfer, $E$, and momentum transfer, $Q$. For hydrogenous systems (e.g., membrane), it is safe to assume that the maximum contribution to the spectra arises from incoherent scattering. This is due to the fact that hydrogen atoms have an overwhelmingly large incoherent scattering cross section, hence practically subduing the scattering signal from other atoms in the system. Here our system of interest is the DHDAB membrane. Hence, to maximize the signal contribution from the DHDAB bilayer in the aqueous system, $D_2O$ is used as the solvent instead of $H_2O$. Nevertheless, to estimate the contribution of solvent itself, QENS data were measured on pure solvent ($D_2O$) as well along with the aqueous solution of vesicles. The scattered intensity corresponding to the DHDAB bilayer can be obtained by subtracting the contribution of solvent ($D_2O$) from the QENS spectra of the aqueous solution of vesicles using the following

equation [21,47]:

$$I_{\rm bl}(Q,E) = I_{\rm solution}(Q,E) - \phi I_{\rm solv}(Q,E), \tag{5}$$

where $\phi$ is the volume fraction of $D_2O$ in vesicles solution, $I_{\rm bl}(Q,E)$, $I_{\rm solution}(Q,E)$, and $I_{\rm solv}(Q,E)$ are measured scattering signals corresponding to DHDAB bilayer, solution of vesicles and solvent, respectively.

The resultant solvent subtracted spectra, $I_{\rm bl}(Q,E)$, are used for data analysis to investigate the diffusion mechanism of the DHDAB molecules. As mentioned earlier, membranes exhibit a hierarchy of dynamics in a wide range of time- and length scales, and the IRIS spectrometer used in this work probes dynamics ranging from nanoseconds to picoseconds. In this time regime, DHDAB molecules perform two distinct motions: (i) lateral motion of the whole molecule within the leaflet of the bilayer and (ii) localized internal motions of the molecule [13]. While both these motions are stochastic in nature and arise due to thermal fluctuations, their relaxation timescales are well separated [13,20]. This allows us to set up the model scattering law for membrane dynamics with the assumption that these motions are independent from each other. The model scattering function of the bilayer is the convolution of scattering function of lateral and internal motion,

$$S_{\rm bl}(Q,E) = S_{\rm lat}(Q,E) \otimes S_{\rm int}(Q,E), \tag{6}$$

where $S_{\rm lat}(Q,E)$ and $S_{\rm int}(Q,E)$ are the scattering functions of the lateral and internal motions of DHDAB molecules in the bilayer, respectively.

Lateral motion relates to the movement of the whole surfactant molecule along the leaflet of the bilayer. Various models including flowlike ballistic motion [51], localized diffusion [66], subdiffusion [54], and Fickian diffusion [52] have been suggested to describe the lateral motion. It has been shown that Fickian diffusion is valid at least for distances greater than a molecule diameter [49,52], which is the case for the length scale accessible by our QENS experiment. The explicit scattering law for lateral motion considering Fickian diffusion is given by a single Lorentzian, which is given by [49,50]

$$S_{\rm lat}(Q,E) = L_{\rm lat}(\Gamma_{\rm lat},E) = \frac{1}{\pi}\frac{\Gamma_{\rm lat}}{(E/\hbar)^2+\Gamma_{\rm lat}^2}, \tag{7}$$

where $\Gamma_{\rm lat}$ is the half-width at half maximum (HWHM) of the Lorentzian function corresponding to the lateral motion. HWHM varies as $D_{\rm lat}Q^2$, where $D_{\rm lat}$ is the lateral diffusion constant.

The general scattering law associated with internal motion of surfactant can be written as

$$S_{\rm int}(Q,E) = A(Q)\delta(E) + (1-A(Q))L_{\rm int}(\Gamma_{\rm int},E). \tag{8}$$

The first term corresponds to the elastic contribution which is characterized by the elastic incoherent structure factor (EISF), $A(Q)$. The second term is the quasielastic contribution described using a Lorentzian function, $L_{\rm int}$ $(\Gamma_{\rm int},E)$ with HWHM, $\Gamma_{\rm int}$. The geometry and relaxation timescale of the internal motion can be obtained from the analysis of the EISF and $\Gamma_{\rm int}$.

Hence, the resultant scattering law for the DHDAB bilayer can be written as

$$S_{\rm bl}(Q,E) = [A(Q)L_{\rm lat}(\Gamma_{\rm lat},E) + (1-A(Q))L_{\rm tot}(\Gamma_{\rm lat}+\Gamma_{\rm int},E)], \tag{9}$$

where $L_{\rm lat}(\Gamma_{\rm lat},E)$ corresponds to the lateral motion and $L_{\rm tot}(\Gamma_{\rm lat+int},E)$ corresponds to the combined lateral and internal motions in the bilayer. The above scattering laws were convoluted with the instrumental resolution function, and the parameters EISF and HWHMs were determined by a least-squares fit of the measured spectra. The data were fitted using the program DAVE [67] developed at the NIST Center for Neutron Research.

### D. Models for internal motion

Internal motions in DHDAB are mainly determined by the molecular structure of the surfactant. Ordering and arrangement of the surfactant molecules in the membrane also play an important role in the nature of the internal motion. DHDAB consists of two hexadecyl alkyl chains ($C_{16}H_{33}$) as the tails and two methyl units in the head group. Hence, internal motions consist of two contributions, the dynamics of methyl units in the head group, and the dynamics of long alkyl tails. With their associated weight factors, the total scattering function corresponding to internal motions can be written as

$$S_{\rm int}(Q,E) = p_h S_{\rm head}(Q,E) + p_t S_{\rm tail}(Q,E), \tag{10}$$

where $S_{\rm head}(Q,E)$ and $S_{\rm tail}(Q,E)$ are the scattering functions corresponding to the head group and alkyl tails, respectively. In the above equation, $p_h$ and $p_t$ are the fractions of hydrogen atoms in head group and alkyl tails, respectively. For the DHDAB molecule ($(C_{16}H_{33})_2N^+(CH_3)_2Br^-$), $p_h$ and $p_t$ are equal to 6/72 and 66/72, respectively. The most probable motion for methyl units in the head group would be the threefold rotation and can be written as [68]

$$S_{\rm head}(Q,E) = \frac{1}{3}[1+2j_0(Qb)]\delta(E) + \frac{1}{\pi}\left[\frac{2}{3}[1-j_0(Qb)]\frac{3\tau_{\rm MG}}{9+E^2\tau_{\rm MG}^2}\right]. \tag{11}$$

Here, $b$ is the H-H distance (1.8 Å) in the methyl group and $\tau_{\rm MG}$ is the mean residence time of a hydrogen atom in methyl unit in head group. The dynamics of alkyl tails strongly depends on the phase state of the membrane [31]. Hence, different models for internal motions for both the ordered and fluid phases of the membrane will be discussed next.

### E. Fractional uniaxial rotational diffusion model

In the coagel phase, DHDAB molecules are well ordered and alkyl chains are all almost in *trans* conformation. In this configuration, the most suitable model for internal motion of the DHDAB will be an uniaxial rotational diffusion (URD) model, in which alkyl chains undergo reorientation on a circle with a radius of gyration $a$. These reorientations are performed by jump rotation with $N$ equivalent sites in the circle large

number $N > 6$ and $Qa \leqslant \pi$. The incoherent scattering law is given by [69]

$$S_{\text{tail}}^{\text{uni}}(Q,E) = B_0(Qa)\delta(E) + \frac{1}{\pi}\sum_{m=1}^{N-1} B_m(Qa)\frac{\tau_m}{1+E^2\tau_m^2} \tag{12}$$

with

$$B_m(Qa) = \frac{1}{N}\sum_{i=1}^{N} j_0\left(2Qa\sin\frac{\pi i}{N}\right)\cos\frac{2\pi mi}{N}.$$

Here, $\tau_m^{-1} = 2\tau_{\text{avg}}^{-1}\sin^2(\frac{m\pi}{N})$, where $\tau_{\text{avg}}$ is the average time spent on the site between two successive jumps and $j_0$ is the Bessel function of zero order. In this case, the rotational diffusion constant $D_{\text{r}}$ can be written as

$$D_r = \frac{2}{\tau_{\text{avg}}}\sin^2\left(\frac{\pi}{N}\right).$$

In the coagel phase, all the hydrogen atoms in the alkyl chain may or may not participate in the internal dynamics. We choose $p_x$ as the fraction of mobile hydrogen atoms in the bilayer undergoing URD, hence the name fractional URD. Including the dynamics of head group, the resultant scattering law for internal motion in the ordered phase can be given by

$$S_{\text{int}}^{\text{ordered}}(Q,E) = A_{\text{ordered}}(Q)\delta(E) + \frac{1}{\pi}\left[\frac{2p_h}{3}[1-j_0(Qb)]\frac{3\tau_{\text{MG}}}{9+\tau_{\text{MG}}^2E^2} + p_xp_t\sum_{m=1}^{N-1}B_m(Qa)\frac{\tau_m}{1+\tau_m^2E^2}\right], \tag{13}$$

where $A_{\text{ordered}}(Q)$ is the EISF of the coagel phase, which can be written as

$$A_{\text{ordered}}(Q) = \frac{p_h}{3}[1+2j_0(Qb)] + p_t(1-p_x) + p_t\left[\frac{p_x}{N}\sum_{i=1}^{N} j_0\left(2Qa\sin\frac{\pi i}{N}\right)\right], \tag{14}$$

In Eq. (14), $p_h = 6/72$ and $p_t = 66/72$. We have taken a sufficiently large number of jump sites $N = 12$ while describing the EISF and HWHM for the ordered phase.

### F. Localized translation diffusion model

As the DHDAB bilayer in the fluid phase is composed of significant disorder, the localized translation diffusion (LTD) model [56,70] is suitable to describe the internal motions in this phase. In this model, it is assumed that the hydrogen atoms in the alkyl chains undergo localized translational diffusion within a sphere. In an alkyl chain, the local degree of mobility can increase and move from the head group region to the tail. Therefore, in the LTD model, we consider a linear distribution of radii and diffusivities, which increase from a minimum value ($R_{\text{min}}$, $D_{\text{min}}$) near the head group and reach a maximum value ($R_{\text{max}}$, $D_{\text{max}}$) near the tail region. The radius and diffusivity of the $i$th particle in the alkyl chain are given by

$$R_i = \frac{i-1}{M-1}[R_{\text{max}} - R_{\text{min}}] + R_{\text{min}}$$

and

$$D_i = \frac{i-1}{M-1}[D_{\text{max}} - D_{\text{min}}] + D_{\text{min}},$$

where $M = 16$ is the total number of $CH_2$ units in the DHDAB alkyl chain. The scattering law for particles diffusing within a sphere is given by Volino and Dianoux [71]. The generalized scattering law for the dynamics of the alkyl chain can be written as [49,71]

$$S_{\text{tail}}^{\text{LTD}}(Q,E) = \frac{1}{M}\sum_{i=1}^{M}\left[A_0^0(QR_i)\delta(E) + \frac{1}{\pi}\sum_{\{l,n\}\neq\{0,0\}}(2l+1) \times A_n^l(QR_i)\frac{\left(x_n^l\right)^2 D_i/R_i^2}{\left[\left(x_n^l\right)^2 D_i/R_i^2\right]^2 + E^2}\right]. \tag{15}$$

In the above equation, the first term is the elastic component $A_0^0(QR_i) = [\frac{3j_1(QR_i)}{QR_i}]^2$ and the second is the quasielastic component $A_n^l(QR_i)(n, l \neq 0, 0)$. Values of $A_n^l$ for different values of $n$ and $l$ can be calculated by using the values of $x_n^l$ listed in Volino and Dianoux [71]. Including the head group dynamics (threefold reorientation), the generalized scattering law for internal motion of DHDAB in the fluid phase will be

$$S_{\text{int}}^{\text{fluid}}(Q,E) = \frac{1}{72}\left[\begin{array}{l}\left\{2(1+2j_0(Qb)) + \frac{66}{M}\sum_{i=1}^{M}\left[\frac{3j_1(QR_i)}{QR_i}\right]^2\right\}\delta(E) \\ +\frac{1}{\pi}\left\{4(1-j_0(Qb))\frac{3\tau_{MG}}{9+E^2\tau_{MG}^2} + \frac{66}{M}\sum_{i=1}^{M}\sum_{\{l,n\}\neq\{0,0\}}(2l+1)A_n^l(QR_i)\frac{(x_n^l)^2D_i/R_i^2}{((x_n^l)^2D_i/R_i^2)^2+E^2}\right\}\end{array}\right]. \tag{16}$$

The resultant EISF for the fluid phase can be written as

$$A_{\text{fluid}}(Q) = \frac{1}{72}\left[2[1+2j_0(Qb)] + \frac{66}{M}\sum_{i=1}^{M}\left[\frac{3j_1(QR_i)}{QR_i}\right]^2\right], \tag{17}$$

where $R_{\text{i}}$ includes $R_{\text{min}}$ and $R_{\text{max}}$, which are the smallest (near the head group) and largest (end point of the tail or far from the head group) radii.

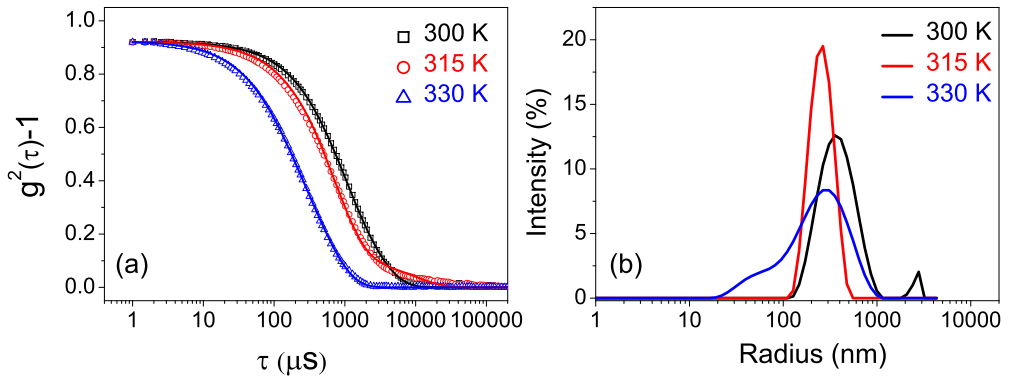


FIG. 2. (a) Intensity autocorrelation functions and (b) size distributions for DHDAB aggregates in $D_2O$ at different temperatures.

## IV. RESULTS AND DISCUSSION

### A. Structure of DHDAB aggregates

The structure of the DHDAB aggregates has been investigated using DLS and SANS. DLS data provide information about the hydrodynamic size of the whole aggregates, whereas the SANS data provide information about the structure of the aggregates. The observed intensity autocorrelation functions are shown in Fig. 2(a). Cumulant analysis suggests PI∼0.3–0.4. Hence, CONTIN analysis [62] has been carried out and the distribution functions in the hydrodynamic size of the aggregates are shown in Fig. 2(b). At 300 K, intensity-weighted distribution of size shows that the hydrodynamic radius of the aggregates is ∼400 nm. A small fraction of large aggregates (∼2600 nm) is also evident. However, as temperature increases, the size-distribution function shifts towards a smaller value suggesting reduction in the size of the aggregates. At 315 K, a size-distribution centered at ∼300 nm is observed. At 330 K, a size-distribution function further shifts towards a lower radius and becomes asymmetric, indicating a notable increase in the population of smaller-sized aggregates.

Observed SANS data for 70 mM DHDAB aggregates in $D_2O$ at 300, 315, and 330 K are shown in Fig. 3. The scattering profiles show $Q^{-2}$ dependence in the low-$Q$ region, which suggests the formation of the unilamellar vesicles (ULVs). The large ULVs are observed as a bilayer in the limited $Q$ range and hence the scattering data are expected to show a linear behavior with a slope of $-2$ on a log-log scale, as in the present case [72]. Moreover, the samples were slightly turbid, which further indicates the formation of the large ULV. It may be added that the formation of multilamellar vesicles has not been considered due to absence of any correlation peak, arising from the repetition of lamella. The SANS data do not show any low-$Q$ cutoff, suggesting that the overall size ($R$+$dR$) of the ULVs is much larger than that corresponding to the $Q$ range of the measurements, as also observed in DLS. Therefore, the overall size ($R$+$dR$) was fixed to a value $> 2\pi/Q_{\min}$ throughout the data analysis. The data analysis carried out using Eqs. (3) and (4) shows a slight decrease in the bilayer layer thickness from 30 to 27 Å, with increasing temperature.

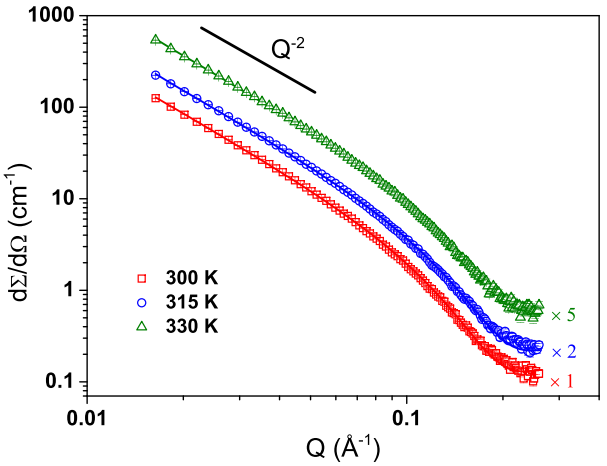


FIG. 3. SANS data for 70 mM DHDAB in $D_2O$ at different temperatures. It is evident that at low $Q$, data show $Q^{-2}$ behavior suggesting lamellar structure. The solid lines are the fits as per the core-shell model discussed in the text. The data are scaled vertically by a multiplicative factor, as shown in figure for clarity.

### B. Phase behavior of DHDAB membrane

Observed DSC thermograms for 70 mM DHDAB vesicles in heating and cooling cycles are shown in Fig. 4. It is evident that during the heating cycle, there are two endothermic peaks at ∼303 and ∼318 K, suggesting DHDAB bilayer undergoes two first-order phase transitions in the heating cycle. The

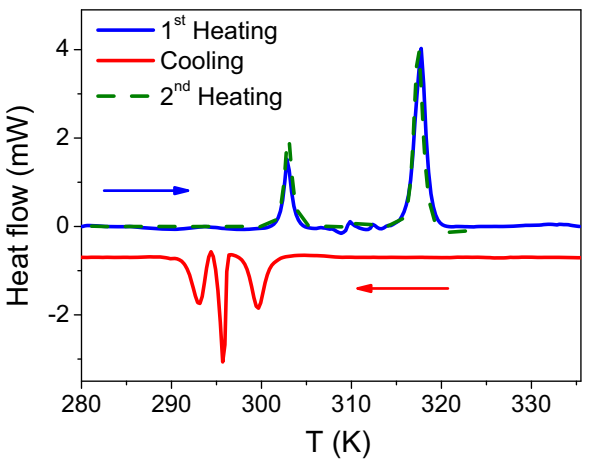


FIG. 4. DSC thermograms for 70 mM DHDAB vesicles in heating and cooling cycles.

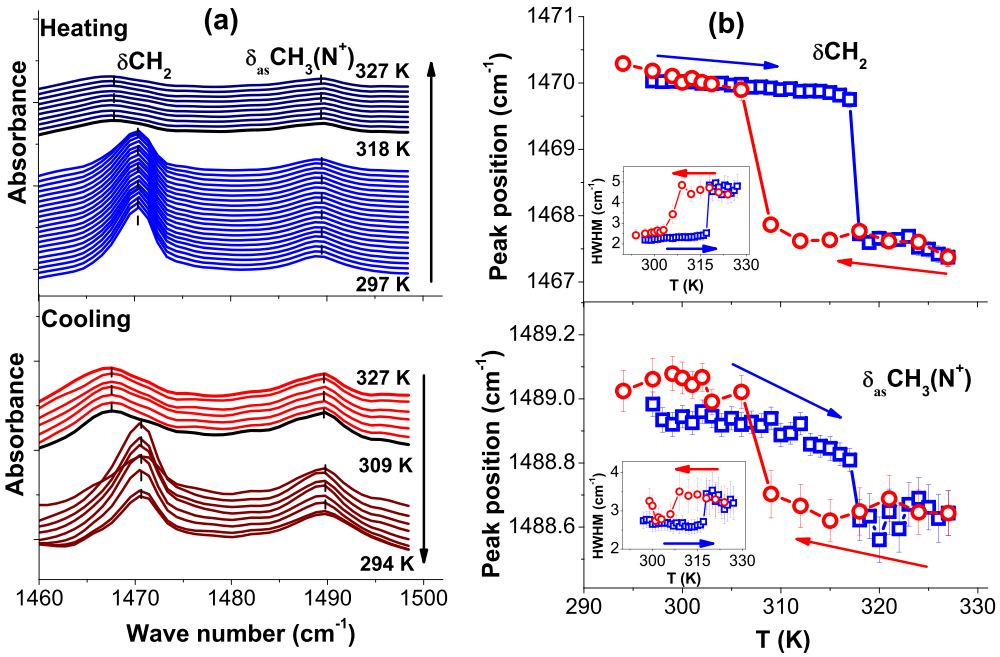


FIG. 5. (a) FTIR absorbance spectra for 70 mM DHDAB in 1460–1500 $cm^{-1}$ spectral region in heating and cooling cycles. Black dashed lines are the guide for the band centers. (b) Temperature-dependent variation of band centers corresponding $\delta CH_2$ and $\delta_{as}CH_3(N^+)$ modes in heating (blue squares) and cooling (red circles) cycles. Temperature-dependent variations of the HWHM corresponding to both the peaks in heating (squares) and cooling (circles) cycles are shown in the insets.

transition at 318 K is relatively stronger (56 kJ/mol) than the transition at 303 K (17.9 kJ/mol). At low temperature, DHDAB forms a coagel phase like DODAB bilayers [13]. DSC results primarily suggest that the system goes from coagel (highly ordered phase) to fluid phase via an intermediate phase. During cooling, the system shows a large hysteresis as the ordering transition occurs at relatively a lower temperature. The reverse transition is observed in the form of three closely spaced peaks, spanning the temperature range of 300 to 293 K. These three closely spaced peaks in the cooling cycle might be due to kinetics of the phase transition or heterogeneity within the membrane. DSC measurements carried out in the second heating cycle are consistent with the first heating, suggesting the system goes back completely into the coagel phase in the cooling cycle. The DSC results obtained here are quite different from those on 2 mM [24,73] and 5 mM [23] DHDAB vesicles, indicating that the phase behavior of DHDAB membrane strongly depends on the concentration of the surfactants. At 2 mM, DHDAB vesicles show a main transition at ∼301 K corresponding to the transition from ordered to fluid phase [24], while at 5 mM, the main phase transition remains unchanged and an extra post-transition at ∼315 K corresponding to the morphological change in the vesicles was also observed [23]. No such post-transition is observed in the present study (70 mM). While comparing the main phase transition temperature ($T_m$) and associated enthalpy ($\Delta H$), it is found that DODAB membrane has relatively higher $T_m$ and associated $\Delta H$ compared to DHDAB [74]. This is consistent with the trend observed for natural phospholipid membranes such as phosphocholine lipid membrane where $T_m$ and associated $\Delta H$ increase with chain length. For example, for dimyristoylphosphatidylcholine (DMPC; $n = 14$) $T_m$ and $\Delta H$ are found to be 297 K and 25 ± 10 kJ/mol, respectively which increases to 328 K and 44 ± 7 kJ/mol for 1,2-distearoyl-sn-glycero-3-phosphocholine (DSPC; $n = 18$) [75].

To examine the nature of these phase transitions, FTIR measurements were carried out in the spectral range 900–4000 $cm^{-1}$. With an aim to characterize the evolution of the hydration and ordering of DHDAB molecules during phase transitions, we focus on the prominent vibrational modes associated with the $N(CH_3)_2^+$ of the head group and $CH_2$ of the alkyl tails. The deformation and stretching vibrations corresponding to these groups are mainly observed in the 1460–1500 $cm^{-1}$ and 2810–2950 $cm^{-1}$ regions, respectively. The 1460–1500 $cm^{-1}$ region contains two absorption bands centered at ∼1470 and 1489 $cm^{-1}$. The former is associated with the $\delta CH_2$ (scissoring) vibrational mode, which is sensitive to the force between the alkyl tails and hence can be used to investigate the packing of the hydrophobic tails [15,76]. The second band in this region is related to asymmetric deformation vibrations of methyl group attached to $N^+$ atom, i.e., $\delta_{as}CH_3(N^+)$ which is known to be sensitive to the extent of disorder and the hydration of head groups [15,17,76].The other region of interest is 2810–2950 $cm^{-1}$, which contains two absorption bands centered at ∼2850 and 2917 $cm^{-1}$ corresponding to $\nu_s CH_2$ (symmetric stretching) and $\nu_{as}CH_2$ (asymmetric stretching) modes, respectively. These bands are sensitive towards the conformational order of the alkyl tails and *trans-gauche* isomerization of the $CH_2$ group in the alkyl tail [15,77].

The observed IR absorbance spectra for DHDAB membrane in the 1460–1500 $cm^{-1}$ spectral region measured at various temperatures in heating as well as cooling cycles have been shown in Fig. 5(a). Two distinct absorption bands corresponding to $\delta CH_2$ and $\delta_{as}CH_3(N^+)$ are evident. Figure 5(b) shows the evolutions of band centers and bandwidths [inset of

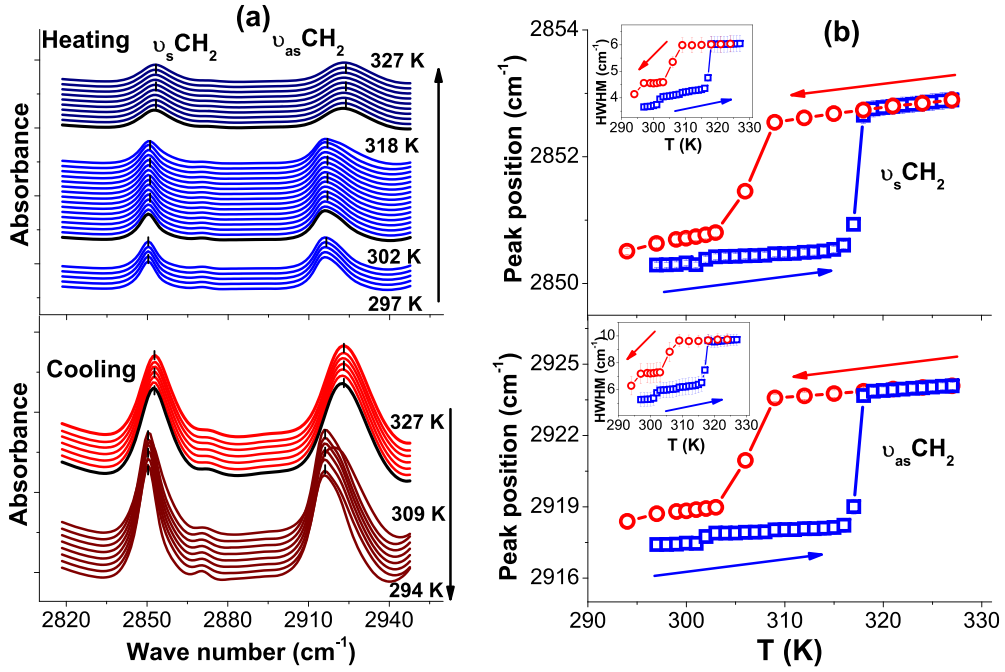


FIG. 6. (a) FTIR absorbance spectra for DHDAB in 2810–2950 $cm^{-1}$ spectral region in heating and cooling cycles. Dashed lines are the guide for the band centers. (b) Temperature-dependent variation of band centers corresponding $\nu_s$ $CH_2$ and $\nu_{as}$ $CH_2$ modes in heating (blue squares) and cooling (red circles) cycles. Temperature-dependent variations of the HWHM corresponding to both the peaks in heating (squares) and cooling (circles) cycles are shown in the insets.

Fig. 5(b)] with temperature as obtained in both heating and cooling cycles for $\delta CH_2$ and $\delta_{as}CH_3(N^+)$ modes. It is evident that at low temperature (297 K), bands corresponding to $\delta CH_2$ and $\delta_{as}CH_3(N^+)$ are relatively sharp and centered at 1470 and 1489 $cm^{-1}$, respectively. The HWHMs of the associated peaks are around 2.2 and 2.7 $cm^{-1}$, respectively. The position and sharpness of the peaks corresponding to $\delta CH_2$ and $\delta_{as}CH_3(N^+)$ suggest that at 297 K DHDAB membrane is in the coagel phase [15]. In the heating cycle, a sudden decrease in the peak positions of both modes is observed at ∼318 K, which corresponds to the phase transition temperature as observed in DSC. The redshift in the $\delta CH_2$ mode across this transition suggests a decrease in the packing density, which can be attributed to an increased disorder in the alkyl tails that is also evident from the increased HWHM [inset of Fig. 5(b)]. The transition at ∼318 K is also marked by a redshift in $\delta_{as}CH_3(N^+)$ mode and increase in its HWHM, suggesting this transition is also accompanied by a significant increase in the hydration and disorder of the head group. This is consistent with the earlier findings that in the crystalline coagel phase, head groups are well ordered and dehydrated [15] and, as the system goes to gel/fluid phase, there is a sudden increase in the hydration and consequently a disorder of the head groups. During the cooling cycle, it is evident that both $\delta CH_2$ and $\delta_{as}CH_3(N^+)$ modes show a large hysteresis, and a discontinuity associated with the ordering transition from the high-temperature phase is observed at ∼309 K.

The FTIR absorbance spectra of DHDAB in the stretching region (2810–2950 $cm^{-1}$) are shown in Fig. 6(a). Two characteristic peaks, corresponding to $\nu_s$ $CH_2$ (symmetric stretching) and $\nu_{as}$ $CH_2$ (asymmetric stretching) modes are observed in this region. The evolution of these band centers and widths in the heating and cooling cycles are plotted in Fig. 6(b). At 297 K, the band centers of $\nu_s$ $CH_2$ and $\nu_{as}$ $CH_2$, are observed at 2850 and 2917 $cm^{-1}$ and the associated peak widths are found to be 3.6 and 5.2 $cm^{-1}$, respectively. A shift in the peak position of these modes corresponds to changes in the ratio of *trans-gauche* isomers and change in the peak width is associated with changes in the rate of *trans-gauche* isomerisation in the alkyl chain. A *gauche* defect is defined as a conformation of the alkyl chain in which the dihedral angle between a set of four consecutive carbon atoms is either 60° or 300°. The introduction of *gauche* defects (i.e., conformational disorder) in the alkyl chains lead to considerable changes in C-H stretching [78], since these modes are highly sensitive to the conformation of alkyl chain [79,80]. Stretching frequencies for *gauche* conformers involve slightly larger energy and therefore occur at a relatively higher frequency compared to the *trans* conformers [77,79]. A small kink in the peak positions [Fig. 6(b)] and peak widths [inset of Fig. 6(b)] of both modes are observed at 303 K. These observations indicate that the first transition observed at 303 K in DSC (heating cycle) is marked by a small increase in alkyl chain disorder, although there is no observable change in the packing of alkyl tails or ordering and hydration state of head group. This transition can thus be associated with a polymorphic transition (solid-solid) where, after the transition, DHDAB bilayers are still in an ordered phase which we refer to from now on as an intermediate crystalline (IC) phase. This resembles the pretransition (gel ripple) observed in phosphocholine membranes [22]. At 318 K, there is a sudden increase in the positions and widths of the peaks corresponding to $\nu_s$ $CH_2$ and $\nu_{as}$ $CH_2$. At 318 K, the peak positions for $\nu_s$ $CH_2$ and $\nu_{as}$ $CH_2$ are observed, ∼2852 and 2924 $cm^{-1}$ [Fig. 6(b)] and peak widths are 6.0

and 9.6 $cm^{-1}$ [inset of Fig. 6(b)], respectively. The blueshift in the stretching frequencies arises due to a large increase in *gauche* defects in the alkyl chain [78]. Further, the increase in the widths indicates that the chains have also become more dynamic with increased isomerization rates at the higher temperature, that is verified by the QENS studies, as discussed in the forthcoming section. These observations suggest that the transition observed at 318 K is the main phase transition where DHDAB membrane goes from the ordered IC phase to the fluid phase. The increase in stretching frequencies across ∼318 K is much larger than that across ∼303 K, suggesting the main phase transition introduces larger number of gauche defects and greater disorder in the membrane compared to the pretransition. In the cooling cycle, the discontinuity in $\nu_s$ $CH_2$ and $\nu_{as}$ $CH_2$ modes of DHDAB is observed at ∼309 K showing a large hysteresis.

The EFWS is an important technique to study the phase transitions associated with the microscopic dynamics. In an EFWS, the neutron elastic intensity is measured (at approximately zero energy transfer as defined by the energy resolution of the spectrometer) as a function of temperature. As temperature increases, the dynamics in the system increase resulting in a loss in the elastic intensity. Any suddent/sharp change in the elastic intensity reveals a significant change in the dynamics and is commonly related to changes in phase. Thus, EFWS provides additional information on phase behaviour complementary to DSC or FTIR. For example, transitions observed in DSC data are related with the change in the enthalpy, making it difficult to ascertain the nature of transition to be due to the structure or the dynamics of the system, whereas in EFWS the observed phase transitions are exclusively associated with the microscopic dynamics of the system. Hence, in order to obtain further insights into the DHDAB phase transitions, EFWS measurements were carried out in heating as well as cooling cycles, and observed data are shown in Fig. 7(a). In the heating cycle, the elastic intensity falls sharply at 303 and 318 K, which suggests that these phase transitions are associated with the change in the microscopic dynamics of the DHDAB bilayer. Below 303 K, the system is in the coagel phase, which is highly ordered, and therefore least dynamic. After the pretransition, some gauche defects get introduced, leading to a notable increase in the dynamics of DHDAB. This transition is associated with the polymorphic (solid-solid) transition. Further, after the main transition, the bilayer goes into the fluid phase, where DHDAB molecules become significantly mobile with a significant number of *gauche* defects. The dynamics of the DHDAB molecules corroborate well with the ordering and packing, as observed from FTIR spectroscopy. The large hysteresis observed in DSC and the behavior of vibrational modes during temperature cycles are also evident in the elastic intensity scan. During the cooling cycle, initially the elastic intensity increases monotonously. At around 297 K, a sharp rise in the elastic intensity is observed which corresponds to the fluid to coagel phase transition, which is consistent with the results of DSC and FTIR spectroscopy.

These results are in sharp contrast with the phase behavior observed for DODAB, a longer-chain counterpart of DHDAB [13]. For direct comparison, the *Q*-averaged EFWS for the DODAB, as obtained with the same experimental setup, is

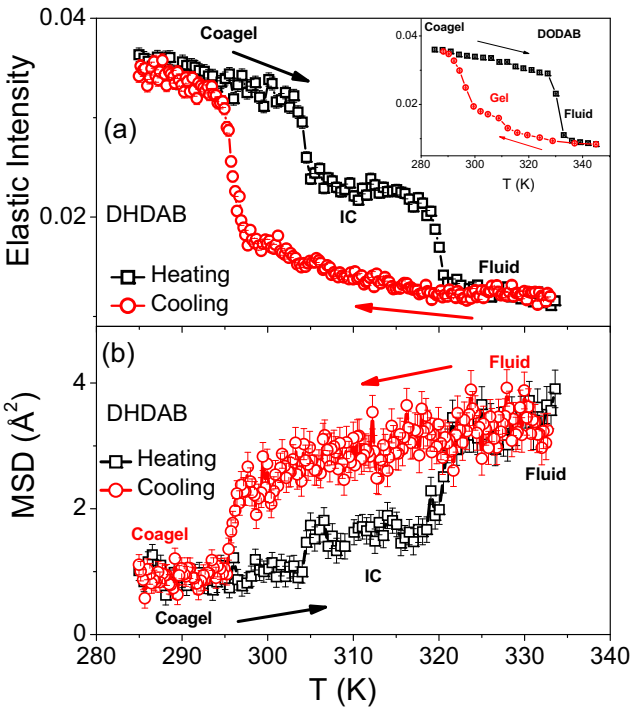


FIG. 7. (a) *Q*-averaged elastic intensity scans for DHDAB vesicle with temperature in both heating and cooling cycles. For direct comparison, *Q*-averaged elastic intensity data for DODAB membrane are shown in the inset. (b) Variation of mean-square displacement (MSD) as obtained from elastic intensity scan for DHDAB bilayer in both heating and cooling cycles. Black squares represent data during heating and red circles correspond to data during cooling cycle. Error bars throughout the text represent one standard deviation.

shown in the inset of Fig. 7(a); the data in the inset of Fig. 7(a) are similar to those reported earlier [13]. In the case of DODAB, during the heating cycle, no pretransition was observed and the DODAB bilayer directly goes to the fluid phase from the coagel phase. Also, in the cooling cycle, it goes back to the coagel phase through an intermediate gel phase. The formation of intermediate gel phase is due to nonsynchronous behavior between the head and tail groups which occurs due to the difference between the interactions experienced between the head groups and tails among them. The tail groups experience mainly the hydrophobic interactions, whereas repulsive Coulombic interaction is the major contributor to the interactions between the head groups. While lowering the temperature, tail groups order prior to the head groups, which results in the formation of an intermediate gel phase. However, in the case of DHDAB, owing to its shorter chain length, no such nonsynchronous behavior is observed in the cooling cycle. On the other hand, a polymorphic (solid-solid) transition from coagel to IC phase is observed for DHDAB in the heating cycle, which is absent in the DODAB. These sharply contrasting phase diagrams for DHDAB and DODAB having only slight difference in molecular structures suggest the strong susceptibility of membrane phase behavior to the alkyl chain length. Such large changes in phase behavior are not observed in more commonly used phospholipids such as

phosphatidylcholine (e.g., DMPC, DPPC, and DSPC), where only an increase in the transition temperature is observed with increasing chain length. It may be noted that the IC phase is different from the intermediate gel phase. In the IC phase, molecules are relatively more ordered and densely packed than those in the intermediate gel phase.

As indicated by FTIR measurements, the phase transitions (coagel-IC and IC-fluid) are marked by significant changes in the alkyl chain conformation. Sharp change in conformational entropy is a key indicator in an order-disorder first-order phase transition. However, the exact calculations of entropy are difficult due to lack of knowledge of the complete conformational space, the correlation between the different motions and the solvent [81]. It is possible however, to estimate the contribution of conformational entropy using neutron scattering, calculating the mean-squared displacement (MSD) of the system at different temperatures [81,82]. The MSDs which quantify the amplitudes of average fluctuations within DHDAB can be calculated from the elastic intensity $I_{el}(Q,T)$ under the Gaussian approximation using $\ln[\frac{I_{el}(Q,T)}{I_{el}(Q,T_{min})}] = -\frac{\langle u^2\rangle Q^2}{3}$. The calculated MSDs in both heating and cooling cycles are shown in Fig. 7(b), indicating distinct phase transitions in the heating and cooling cycles, as observed in the $Q$-averaged elastic intensity scans. The change of conformational entropy $\Delta S_{conf}$ in proteins due to folding/unfolding or binding of the ligand [81,82] has been calculated using the MSD estimated from neutron scattering. In this study, we have adapted this method to estimate the $\Delta S_{conf}$ across different phase transitions. The hysteresis in the phase behavior of DHDAB bilayer enables us to have different phases at the same temperature. In our calculations, we have considered the comparison between coagel and fluid phases at 300 K and comparison between IC and fluid phase at 315 K. In this bilayer system, it is safe to assume that the $CH_2$ group of the alkyl chain is the smallest individual mobile unit, which explores the conformational space associated with the dynamics observed within the resolution of the QENS spectrometer. The change in the conformational entropy per $CH_2$ unit during the phase transitions from the MSD is calculated using the given formula [82],

$$\Delta S_{conf} = 3R \ln\left(\sqrt{\frac{\langle u^2\rangle_{fluid}}{\langle u^2\rangle_{coagel/IC}}}\right), \tag{18}$$

where $R$ is the universal gas constant (8.3144 J $K^{-1}$ $mol^{-1}$). The estimated $\Delta S_{conf}$ for the coagel-fluid and IC-fluid phase transitions are found to be 11.9 and 7.6 J $K^{-1}$ $mol^{-1}$, respectively. The sharp increase in entropy is an indicator of increased disorder in the alkyl chain conformations of the DHDAB molecules.

### C. Microscopic dynamics of DHDAB membrane

Elastic intensity scan reveals that phase transitions in DHDAB membrane are associated with the notable changes in the microscopic dynamics of the bilayer. QENS measurements were carried out at different temperatures to investigate the detailed mechanism of microscopic dynamics across the different phases. Temperatures of the measurements were decided based on the elastic scan results. The measurements

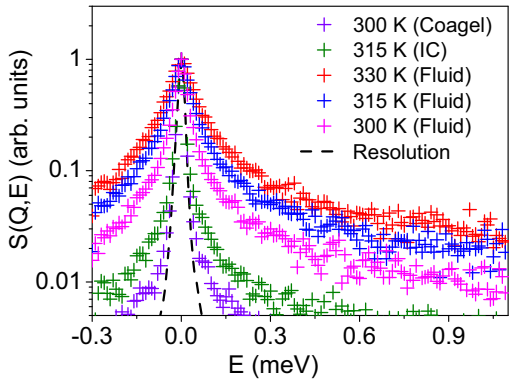


FIG. 8. Observed QENS spectra for the DHDAB bilayer at $Q = 1.22$ Å$^{-1}$ in different phases. The contribution of the solvent ($D_2O$) is subtracted, and the resultant spectra are peak normalized. Instrument resolution as measured from standard vanadium is shown by a dashed line.

were carried out at temperatures of 300 K (coagel), 315 K (IC), and 330 K (fluid) during the heating cycle and at 315 K (fluid) and 300 K (fluid) during the cooling cycle. The presence of a large hysteresis in the heating and cooling cycles gives an opportunity to investigate solely the effects of the phase state of the bilayer on the membrane dynamics. For example, a comparison of the QENS spectra at 315 K (heating cycle) and 315 K (cooling cycle) gives information on the difference in dynamics is between the crystalline and fluid phases. Figure 8 shows the observed QENS spectra corresponding to DHDAB bilayer at different temperatures at a typical $Q$ value of 1.22 Å$^{-1}$. The instrumental resolution as measured using standard a vanadium sample is also shown in Fig. 8. For direct comparison of the broadening in the QENS spectra, all the data have been peak normalized. Mobility of DHDAB molecules is directly related to the quasielastic (QE) broadening in the QENS spectra. The ordered phase (300 and 315 K during the heating cycle) showed less QE broadening compared to the other phases, suggesting membrane dynamics is restricted in the ordered phase. As the temperature increases to 330 K, there is a sudden jump in the QE broadening suggesting a sharp enhancement in the membrane dynamics across the main phase transition, consistent with the elastic intensity scan data and DSC measurements. As the temperature is lowered (in cooling cycle), QENS spectra for 315 and 300 K are much broader than those observed for the same temperatures in the heating cycle. Moreover, no sudden decrease in the QE broadening is observed, suggesting that during the cooling cycle, DHDAB membrane is still in the fluid phase, up to 300 K. This is consistent with the described phase behavior of the DHDAB bilayer, which showed a large hysteresis with fluid to coagel transition occurring at ∼298 K during the cooling cycle as observed in EFWS measurements.

FTIR measurements indicate the coagel and IC phases are much more ordered with tightly packed structures, as compared to the fluid phase. Therefore, the lateral motion of DHDAB is too slow to be resolved by the QENS spectrometer used here. This is also supported by the fact that the scattering law [Eq. (8)] corresponding to internal motion of the DHDAB could solely describe the observed QENS spectra at 300 K

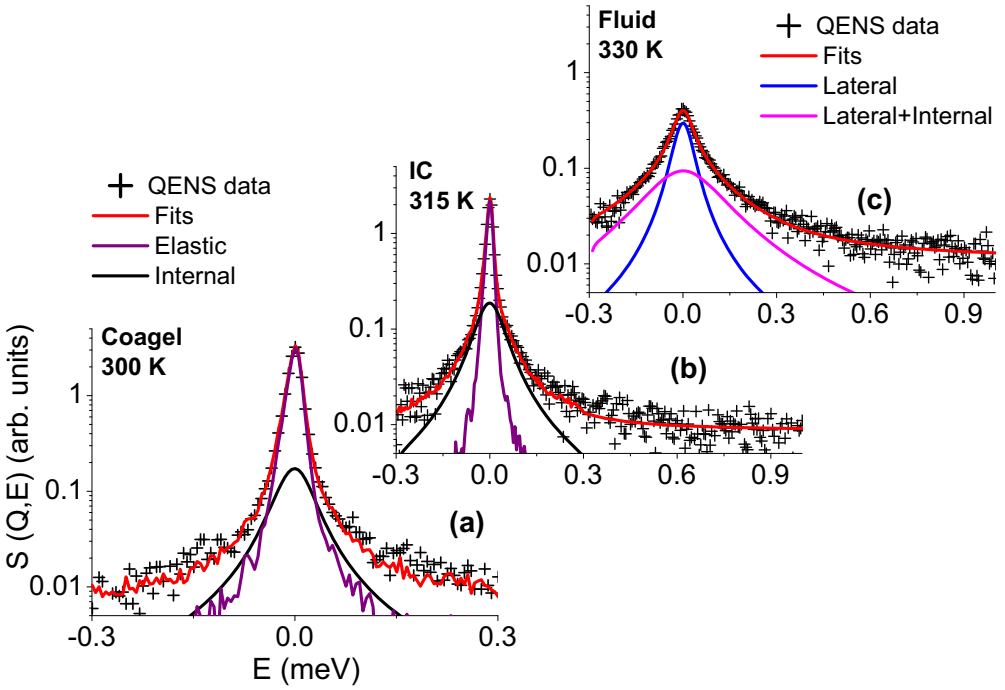


FIG. 9. Typical fitted QENS spectra of DHDAB bilayer in the coagel (300 K), IC (315 K), and fluid (330 K) phases at $Q = 1.22$ Å$^{-1}$.

(coagel) and 315 K (IC). Typical fitted QENS spectra for the coagel (300 K) and IC (315 K) phases are shown in Figs. 9(a) and 9(b). The elastic and quasielastic components associated with the internal motion are also indicated in the figure. In the fluid phase, which has a low packing density aided by significant alkyl chain disorder, both lateral and internal motions are observed. Hence, the QENS spectra in the fluid phase are modeled considering a convolution of their respective scattering functions, as given in Eq. (9). Figure 9(c) shows a typical QENS spectrum of DHDAB bilayer at 330 K, along with the respective model fits based on Eq. (9). The Lorentzian components corresponding to lateral and (lateral+internal) motion are also indicated in figure. The detailed analysis describing the nature and timescale of motions using the obtained parameters is described below.

### D. Ordered phases

The variations of the obtained fit parameters EISF and $\Gamma_{\text{int}}$ with respect to $Q$, characterize the nature of the internal motion. Figure 10(a) shows the EISF obtained for the coagel and IC phases from the QENS fitting [Eq. (8)]. It is apparent that at higher $Q$, the EISF of these two phases saturate to a constant value, which indicates the existence of an immobile fraction in the system. In coagel or IC phase, alkyl chains are highly ordered and almost in all *trans* conformation. Therefore, in both these phases, we found that the fractional URD model is best suited to describe the internal motions of the alkyl tails. The EISF for these ordered phases were fit with Eq. (14) to extract $p_x$ and $a$, which represent the mobile fraction and radius of gyration of the hydrogen atoms performing the URD, respectively. The radius of gyration, $a$, is found to be 1.6 ± 0.2 Å in the coagel phase and 1.9 ± 0.3 Å in the IC phase. The modest increase in $a$ can be ascribed to the mild increase in the alkyl chain disorder in the system, as observed from FTIR measurements. On the other hand, it is observed that the fraction of mobile hydrogen doubles from 20 to 40% as the bilayer transitions from coagel to IC phase. This is also evident from the sharp decline in elastic scan at ∼303 K associated with coagel-IC phase transition. Figure 10(b) shows

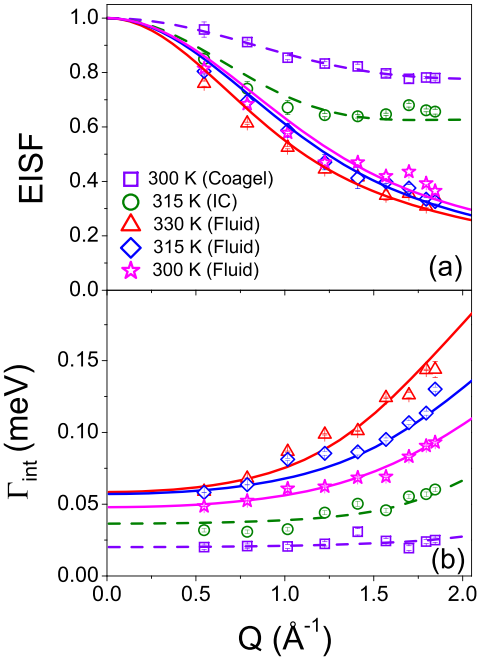


FIG. 10. Variations of (a) EISF and (b) HWHM corresponding to internal motion in different phases. Dashed and solid lines are the fits corresponding to fractional uniaxial rotational and localized transitional diffusion models, respectively.

TABLE I. Dynamical parameters for internal motion as obtained from the analysis of the QENS data at different temperatures in the fluid phase of the DHDAB bilayer.

| | | $D_{int} \times 10^{-6}$ (cm$^2$/s) | | |
|---|---|---|---|---|
| Temperature (K) | $R_{max}$ (Å) | $D_{min}$ | $D_{max}$ | $\tau_{MG}$ (ps) |
| 330 | 3.3 ± 0.4 | 0.5 ± 0.2 | 17.9 ± 1.4 | 4.1 ± 0.2 |
| 315 | 2.8 ± 0.4 | 0.6 ± 0.2 | 12.6 ± 1.4 | 4.6 ± 0.2 |
| 300 | 2.7 ± 0.3 | 0.3 ± 0.1 | 9.8 ± 0.7 | 4.9 ± 0.3 |

the plot of $\Gamma_{int}$ obtained for coagel and IC phases, along with the least-square fits calculated based on Eq. (13). The rotational diffusion constant of the DHDAB molecules is found to $3.0(\pm 0.3) \times 10^{10}$ s$^{-1}$ and $5.5(\pm 0.5) \times 10^{10}$ s$^{-1}$ in the coagel and IC phases, respectively. This is consistent with the observations of symmetric/asymmetric stretching bands of $CH_2$ in FTIR which showed the augmentation of rotational motion of DHDAB molecules across the coagel-IC phase transition. The mean residence times of threefold reorientation of methyl units in the head group is found to 6.9 ± 0.3 ps and 6.8 ± 0.2 ps, respectively, substantiating the FTIR observation that there is no significant change in the head group hydration/dynamics across the polymorphic coagel-IC phase transition.

### E. Fluid phase

Above the main phase transition temperature (∼318 K), the hydrocarbon tails are more disordered with significant *gauche* defects. The increase in disorder and low packing density will enable the alkyl chains in the fluid phase to perform various kinds of internal motions like chain reorientations, bending modes, stretching modes, and so on. A superposition of these motions could be modeled using a LTD in which the hydrogen atoms of the $CH_2$ group undergo localized motion within spherical domains. The EISF of the internal motion for the fluid phase at 300, 315, and 330 K are shown in Fig. 10(a). It is apparent from the qualitative nature of the curve that the geometry of the internal dynamics in the fluid phase is starkly different from that of the ordered phases. This can be quantified by using the LTD model described in the analysis section, where the $Q$ dependence of the EISF, $A(Q)$, is given by Eq. (17). In this model the hydrogen atoms are diffusing within spheres of varying radii which increase linearly from the head group to tail. The least-square fits of this model for the experimental EISF are shown in Fig. 10(a). The obtained values of the maximum radius of localization ($R_{max}$) are given in Table I. It is found that at $T = 300$ K (fluid) $R_{max} = 2.7 \pm 0.3$ Å, which increases with temperature and is found to be 3.3 ± 0.4 Å at 330 K (fluid). The HWHM of internal motion, $\Gamma_{int}$ for the fluid phase at three different temperatures is shown in Fig. 10(b). The saturation of the HWHM at low $Q$ is a signature of localization of the dynamics. The least-square fits of $\Gamma_{int}$ based on LTD model are also shown in Fig. 10(b), from which the maximum and minimum diffusivities are extracted and listed in Table I. It is evident that both the spatial and temporal aspects of the internal motion are sensitive to the temperature of the system.

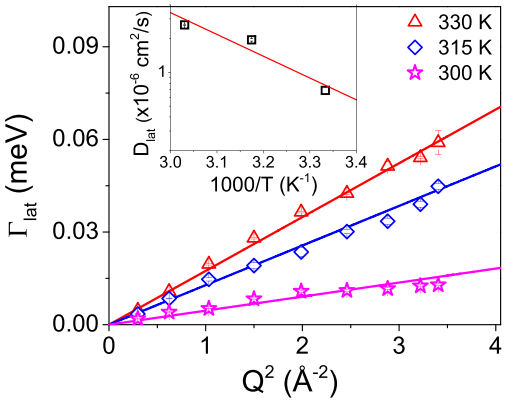


FIG. 11. Variation of HWHM of Lorentzian corresponding to the lateral motion with $Q^2$ at different temperatures. Solid lines are the fits based on Fickian diffusion. Arrhenius plot of lateral diffusion coefficient is shown in the inset. The solid line corresponds to the fit based on the Arrhenius law.

As mentioned earlier, in the fluid phase, an additional motion, lateral motion of the DHDAB molecules within the leaflet, is observed. This motion is of paramount interest due to its significant role in various physiologically relevant processes such as cell signaling, membrane-protein interaction, permittivity, and endocytosis [25] and plays a vital role in maintaining the fluidity of the cell membrane. The HWHM associated with lateral motion, $\Gamma_{lat}$, is shown in Fig. 11 for the DHDAB bilayer in the fluid phase at 300, 315, and 330 K. The linear dependence of $\Gamma_{lat}$ with respect to $Q^2$ indicates that the lateral diffusion is Fickian in nature. The lateral diffusivity, $D_{lat}$, is extracted from least-square fits of $\Gamma_{lat} = D_{lat}Q^2$.The theoretical fits are also indicated in Fig. 11 by solid lines. The lateral motion becomes more than three times faster across a temperature rise of 330 K. $D_{lat}$ at 300 K is found to be $0.7 \times 10^{-6}$(cm$^2$/s) and increases to $2.7 \times 10^{-6}$ (cm$^2$/s) and 330 K. The temperature sensitivity of the lateral diffusion can be characterized through the Arrhenius equation for $D_{lat}$, given by, $D_{lat} = D^0_{lat} e^{-[(E_A)/(k_B T)]}$, where $E_A$ is the activation energy, $k_B$ is the Boltzmann constant, and $T$ is the temperature of the system. The Arrhenius fits are shown in the inset of Fig. 11. The obtained activation energy is found to be ∼37 ± 6 kJ/mol.

To conclude, we make a prudent comparison of the DHDAB dynamics with its counterparts, namely, DODAB [13] and 1,2-dipalmitoylphosphatidylglycerol (DPPG) [46]. In comparison with DODAB, we aim to bring out the effects of the alkyl chain length on the dynamics and with DPPG, the comparison can make out the effects of the head group. It has to be noted that the phase behaviors of all these three molecules are starkly different and therefore the comparison has to be carried between appropriate phases. In the ordered crystalline phase, at 315 K, dynamics of both DHDAB and DODAB molecules can be well described with a fractional uniaxial rotational model. While the fraction of mobile atoms in DHDAB (40%) is more than two times that observed in DODAB (15%), the rotational diffusion constants are quite similar [13], indicating that the shorter chain length possibly leads to looser chain packing the crystalline phase

due to weaker hydrophobic interaction. This in turn leads to an increase in the mobile fraction. In the fluid phase, the internal motion of DHDAB and DODAB molecules is quite similar as both the systems follow localized translational diffusion mechanism with comparable diffusivities. However, the lateral motion is faster in the case of DHDAB as compared to DODAB [13,32]. For example at 330 K (fluid phase), $D_{\text{lat}}$ for DODAB [32] and DHDAB membrane were found to be $2.2(\pm 0.1) \times 10^{-6}\,\text{cm}^2/\text{s}$ and $2.7(\pm 0.1) \times 10^{-6}\,\text{cm}^2/\text{s}$, respectively. The higher diffusivity in case of DHDAB membrane can be attributed to two major underlying reasons—more loose packing in DHDAB membrane and lower size and mass of the DHDAB molecule. Results are also compared with the anionic DPPG lipid membrane [46], which has the same tail length as DHDAB but a different head group. As no crystalline phase is formed in DPPG, we only compare the dynamical behavior in the fluid phase (at 330 K). It is found that lateral diffusivity of DHDAB is at least ∼1.5 times greater than that of DPPG ($1.7 \times 10^{-6}\,\text{cm}^2/\text{s}$) [46]. Lateral diffusion in a bilayer is a complex process depending on various factors like area per lipid (APL), nature of molecular interaction, molecular structure, obstructions, etc. [22,83–85]. Although APL plays a dominant role in controlling the lateral mobility, using the flexible strings model, recently it has been shown that entropic repulsive forces between lipids can also contribute independently to change in lateral motions of the lipids [57]. Despite having very similar APL (∼67 Å$^2$ at 323 K) [85,86], the observed difference in the lateral diffusivities of DHDAB and DPPG molecules emphasizes the roles of molecular structure and interaction on the membrane dynamics.

## V. CONCLUSIONS

Cationic double-chained surfactants have attracted a great deal of attention, not only for fundamental understanding of dynamical and phase behavior of membrane, but also for their widespread applications such as in the domain of nonviral gene delivery systems. These systems show a rich phase behavior, which strongly depends on the concentration of the surfactants, counterions, pH, etc. Here, we have investigated the structural, dynamical and phase behavior of 70 mM dihexadecyldimethylammonium bromide (DHDAB), in the temperature range 290–330 K. SANS, DLS, DSC, FTIR, and neutron EFWS measurements were carried out. SANS and DLS measurements suggest that DHDAB aggregates form large-sized unilamellar vesicles. DSC, FTIR, and EFWS measurements reveal that at low temperatures, DHDAB bilayer forms the coagel phase. During the heating cycle, two distinct first-order transitions corresponding to a pretransition (coagel-IC phase) and a main transition (IC-fluid phase) are observed at 303 and 318 K, respectively. However, in the cooling cycle, a large hysteresis is observed and the fluid phase directly goes back to the coagel phase. This is in sharp contrast with the phase behavior of 70 mM dioctadecyldimethylammonium bromide (DODAB) [13], a longer-chain kin of DHDAB. In the heating cycle, no pretransition is observed and DODAB membrane directly goes to the fluid phase from the coagel phase, but in the cooling cycle, it goes back to the coagel phase via an intermediate gel phase. Occurrence of an intermediate gel phase is attributed to the nonsynchronous behavior of charged head group and hydrophobic tails, which arises due to the differences in the nature of head-head and tail-tail interactions. However, in the case of DHDAB, owing to its shorter chain length, no such nonsynchronous behavior is observed in the cooling cycle, as the head group and tail get ordered simultaneously in the cooling process. On the other hand, a polymorphic phase transition (coagel-IC) is observed for DHDAB in the heating cycle, in which only the tail gets slightly disordered. FTIR and EFWS measurements clearly reveal that all the observed transitions are accompanied with significant changes in the microscopic dynamics of the membrane.

QENS measurements revealed detailed characteristics of the membrane dynamics. In the coagel and IC phases, only localized internal motions are observed, which is expected due to higher ordering of the surfactants molecules. However, in the fluid phase both long-range lateral motion and localized internal motions are observed. The nature of the internal motion is strongly governed by the phase state of the membrane, showing that it is significantly dependent on both the packing density and *gauche* defects. While the loose packing in the fluid phase can be attributed to the strong enhancement of the lateral motion, the increased *gauche* defects and isomerization rate might be the cause of starkly different models for internal motion. In view of this, the results from FTIR compare well with the QENS experimental findings, highlighting an intricate structure-dynamics relationship in membranes. In a recent study of lateral diffusion based on the flexible strings model, it has been noted that the increase in lateral diffusivity across the phase transition is not only due to the increase in area per lipid but also due to a change in the entropic repulsive force between lipids [57]. Our observations about the change in lateral diffusion and conformational entropy across the phase transition support the predictions given by the flexible strings model. Among its counterparts with analogous alkyl chain (DPPG, etc.), it is found that the lateral motion of DHDAB in the fluid phase is the fastest. This might be a helpful characteristic of DHDAB in determining the release kinetics of the drugs or DNA in biomedical applications.

[1] A. Tasset, A. Bellamkonda, W. Wang, I. Pyatnitskiy, D. Ward, N. Peppas, and H. Wang, Nanoscale **14**, 3698 (2022).
[2] K. Bulaklak and C. A. Gersbach, Nat. Commun. **11**, 5820 (2020).
[3] C. E. Dunbar, K. A. High, J. K. Joung, D. B. Kohn, K. Ozawa, and M. Sadelain, Science **359**, 175 (2018).
[4] I. Lostalé-Seijo and J. Montenegro, Nat. Rev. Chem. **2**, 258 (2018).
[5] B. Martin, M. Sainlos, A. Aissaoui, N. Oudrhiri, M. Hauchecorne, P. J. Vigneron, M. J. Lehn, and P. Lehn, Curr. Pharm. Des. **11**, 375 (2005).
[6] H. Zu and D. Gao, AAPS J. **23**, 78 (2021).
[7] H. Yin, R. L. Kanasty, A. A. Eltoukhy, A. J. Vegas, J. R. Dorkin, and D. G. Anderson, Nat. Rev. Genet. **15**, 541 (2014).
[8] P. Lehn, S. Fabrega, N. Oudrhiri, and J. Navarro, Adv. Drug. Deliv. Rev. **30**, 5 (1998).

[9] C. Pennetta, N. Bono, F. Ponti, M. C. Bellucci, F. Viani, G. Candiani, and A. Volonterio, Bioconjugate Chem. **32**, 690 (2021).

[10] J. Buck, P. Grossen, P. R. Cullis, J. Huwyler, and D. Witzigmann, ACS Nano **13**, 3754 (2019).

[11] R. Koynova and B. Tenchov, Top. Curr. Chem. **296**, 51 (2010).

[12] E. Sackmann, Handbook of Biological Physics **1**, 213 (1995).

[13] P. S. Dubey, H. Srinivasan, V. K. Sharma, S. Mitra, V. G. Sakai, and R. Mukhopadhyay, Sci. Rep. **8**, 1862 (2018).

[14] P. Gill, T. T. Moghadam, and B. Ranjbar, J. Biomol. Tech. **21**, 167 (2010).

[15] F.-G. Wu, N.-N. Wang, and Z.-W. Yu, Langmuir **25**, 13394 (2009).

[16] F.-G. Wu, Z.-W. Yu, and G. Ji, Langmuir **27**, 2349 (2011).

[17] T. C. Wong, N. B. Wong, and P. A. Tanner, J. Colloid Interface Sci. **186**, 325 (1997).

[18] R. N. A. H. Lewis, D. Zweytick, G. Pabst, K. Lohner, and R. N. McElhaney, Biophys. J. **92**, 3166 (2007).

[19] M. A. Kamal, A. Pal, V. A. Raghunathan, and M. Rao, Phys. Rev. E **85**, 051701 (2012).

[20] V. K. Sharma, H. Srinivasan, V. García Sakai, and S. Mitra, J. Appl. Phys. **128**, 154701 (2020).

[21] V. K. Sharma, S. Ghosh, P. Mandal, T. Yamada, K. Shibata, S. Mitra, and R. Mukhopadhyay, Soft Matter **13**, 8969 (2017).

[22] V. K. Sharma, E. Mamontov, M. Tyagi, S. Qian, D. K. Rai, and V. S. Urban, J. Phys. Chem. Lett. **7**, 2394 (2016).

[23] E. Feitosa, J. Jansson, and B. Lindman, Chem. Phys. Lipids **142**, 128 (2006).

[24] M. J. Blandamer, B. Briggs, P. M. Cullis, S. D. Kirby, and J. B. F. N. Engberts, J. Chem. Soc. Faraday Trans. **93**, 453 (1997).

[25] D. H. W. Hubert, M. Jung, P. M. Frederik, P. H. H. Bomans, J. Meuldijk, and A. L. German, Langmuir **16**, 8973 (2000).

[26] P. Saveyn, P. Bomans, P. Frederik, M. D. Cuyper, and P. V. Meeren, Langmuir **23**, 4775 (2007).

[27] P. Singh, S. Choudhury, V. K. Sharma, S. Mitra, R. Mukhopadhyay, R. Das, and S. K. Pal, ChemPhysChem **19**, 2709 (2018).

[28] P. Singh, D. Mukherjee, S. Singha, V. K. Sharma, I. I. Althagafi, S. A. Ahmed, R. Mukhopadhyay, R. Das, and S. K. Pal, RSC Adv. **9**, 35549 (2019).

[29] P. S. Dubey, V. K. Sharma, H. Srinivasan, S. Mitra, V. G. Sakai, and R. Mukhopadhyay, J. Phys. Chem. B **122**, 9962 (2018).

[30] P. Saveyn, P. V. Meeren, M. Zackrisson, T. Narayanan, and U. Olsson, Soft Matter **5**, 1735 (2009).

[31] V. K. Sharma, H. Srinivasan, V. García Sakai, and S. Mitra, Struct. Dyn. **7**, 051301 (2020).

[32] P. Singh, V. K. Sharma, S. Singha, V. García Sakai, R. Mukhopadhyay, R. Das, and S. K. Pal, Langmuir **35**, 4682 (2019).

[33] I. Tucker, J. Penfold, R. Thomas, I. Grillo, J. Barker, and D. Mildner, Langmuir **24**, 6509 (2008).

[34] I. Tucker, J. Penfold, R. Thomas, I. Grillo, D. Mildner, and J. Barker, Langmuir **24**, 10089 (2008).

[35] W. T. Li, Y. M. Yang, and C. H. Chang, Colloids Surf. B: Biointerfaces **66**, 187 (2008).

[36] S. Song, P. Fu, Y. Wang, Z. Wang, and Y. Qian, Colloids Surf. A **399**, 100 (2012).

[37] I. Tucker, J. Penfold, R. K. Thomas, I. Grillo, J. G. Barker, and D. F. R. Mildner, Langmuir **24**, 7674 (2008).

[38] J. Lee and C.-H. Chang, Soft Matter **10**, 1831 (2014).

[39] M. Schmid, C. Wölk, J. Giselbrecht, K. A. Chan, and R. D. Harvey, Colloids Surf. B **169**, 298 (2018).

[40] C.-H. Chang, C.-H. Liang, Y.-Y. Hsieh, and T.-H. Chou, J. Phys. Chem. B **116**, 2455 (2012).

[41] I. Tucker, J. Penfold, R. K. Thomas, and I. Grillo, Langmuir **25**, 2661 (2009).

[42] J. Perlo, C. J. Meledandri, E. Anoardo, and D. F. Brougham, J. Phys. Chem. B **115**, 3444 (2011).

[43] A. A. Nevzorov, T. P. Trouard, and M. F. Brown, Phys. Rev. E **55**, 3276 (1997).

[44] R. Macháň, and M. Hof, and - BBA, Biomembranes **1798**, 1377 (2010).

[45] H. M. McConnell and R. D. Kornberg, Biochemistry **10**, 1111 (1971).

[46] J. Bhatt Mitra, V. K. Sharma, A. Mukherjee, V. Garcia Sakai, A. Dash, and M. Kumar, Langmuir **36**, 397 (2020).

[47] S. Qian, V. K. Sharma, and L. A. Clifton, Langmuir **36**, 15189 (2020).

[48] S. Gupta and R. Ashkar, Soft Matter **17**, 6910 (2021).

[49] V. K. Sharma, E. Mamontov, D. B. Anunciado, H. O'Neill, and V. Urban, J. Phys. Chem. B **119**, 4460 (2015).

[50] V. K. Sharma, E. Mamontov, D. B. Anunciado, H. O'Neill, and V. S. Urban, Soft Matter **11**, 6755 (2015).

[51] S. Busch, C. Smuda, L. C. Pardo, and T. Unruh, J. Am. Chem. Soc. **132**, 3232 (2010).

[52] C. L. Armstrong, M. Trapp, J. Peters, T. Seydel, and M. C. Rheinstädter, Soft Matter **7**, 8358 (2011).

[53] C.-Z. Xie, S.-M. Chang, E. Mamontov, L. R. Stingaciu, and Y.-F. Chen, Phys. Rev. E **101**, 012416 (2020).

[54] E. Flenner, J. Das, M. C. Rheinstädter, and I. Kosztin, Phys. Rev. E **79**, 011907 (2009).

[55] J.-H. Jeon, H. Martinez-Seara Monne, M. Javanainen, and R. Metzler, Phys. Rev. Lett. **109**, 188103 (2012).

[56] S. Mitra, V. K. Sharma, V. Garcia-Sakai, A. Orecchini, T. Seydel, M. Johnson, and R. Mukhopadhyay, J. Phys. Chem. B **120**, 3777 (2016).

[57] B. Kheyfets, T. Galimzyanov, and S. Mukhin, Phys. Rev. E **99**, 012414 (2019).

[58] V. K. Aswal and P. S. Goyal, Current Science **79**, 947 (2000).

[59] C. Carlile and M. A. Adams, Physica B **182**, 431 (1992).

[60] O. Arnold, J. C. Bilheux, J. M. Borreguero, A. Buts, S. I. Campbell, L. Chapon, M. Doucet, N. Draper, R. Ferraz Leal, M. A. Gigg *et al.*, Nucl. Instrum. Methods. Phys. Res. A **764**, 156 (2014).

[61] D. E. Koppel, J. Chem. Phys. **57**, 4814 (1972).

[62] S. W. Provencher, Comput. Phys. Commun. **27**, 229 (1982).

[63] J. B. Hayter and J. Penfold, Colloid Polym. Sci. **261**, 1022 (1983).

[64] J. S. Pedersen, Adv. Colloid Interface Sci. **70**, 171 (1997).

[65] P. R. Bevington, *Data Reduction and Error Analysis for Physical Sciences* (McGraw-Hill, New York, 1969).

[66] U. Wanderlingh, G. D'Angelo, C. Branca, V. Conti Nibali, A. Trimarchi, S. Rifici, D. Finocchiaro, C. Crupi, J. Ollivier, and H. D. Middendorf, J. Chem. Phys. **140**, 174901 (2014).

[67] R. T. Azuah, L. R. Kneller, Y. Qiu, P. L. W. Tregenna-Piggott, C. M. Brown, J. R. D. Copley, and R. M. Dimeo, J. Res. Natl. Inst. Stand. Technol. **114**, 341 (2009).

[68] M. Bee, *Quasielastic Neutron Scattering* (Adam Hilger, Bristol, UK, 1988).

[69] A. Dianoux, F. Volino, and H. Hervet, Mol. Phys. **30**, 1181 (1975).
[70] V. K. Sharma, S. Mitra, G. Verma, P. Hassan, V. Garcia Sakai, and R. Mukhopadhyay, J. Phys. Chem. B **114**, 17049 (2010).
[71] F. Volino and A. Dianoux, Mol. Phys. **41**, 271 (1980).
[72] R. Kaur, S. Kumar, V. K. Aswal, and R. K. Mahajan, Langmuir **29**, 11821 (2013).
[73] A. Kacperska, J. Therm. Anal. Calorim. **61**, 63 (2000).
[74] R. A. Gonçalves, Y.-M. Lam, and B. Lindman, Molecules **26**, 3946 (2021).
[75] R. Koynova and M. Caffrey, Biochim. Biophys Acta **1376**, 91 (1998).
[76] W. Wang, L. M. Li, and S. Q. Xi, J. Colloid Interface Sci. **155**, 369 (1993).
[77] A. Nabet, M. Auger, and M. Pezolet, Appl. Spectrosc. **54**, 948 (2000).
[78] H. L. Casal and H. H. Mantsch, Biochim. Biophys. Acta **779**, 381 (1984).
[79] Z. Kota, M. Debreczeny, and B. Szalontai, Biospectroscopy **5**, 169 (1999).
[80] V. R. Kodati and M. Lafleur, Biophys. J. **64**, 163 (1993).
[81] J. Fitter, Biophys. J. **84**, 3924 (2003).
[82] M. Sarter, D. Niether, B. W. Koenig, W. Lohstroh, M. Zamponi, N. H. Jalarvo, S. Wiegand, J. Fitter, and A. M. Stadler, J. Phys. Chem. B **124**, 324 (2020).
[83] M. J. Saxton, Curr. Top. Membr. **48**, 229 (1999).
[84] B. Korchowiec, A. Stachowicz-Kuśnierz, and J. Korchowiec, Environ. Sci.: Processes Impacts **21**, 438 (2019).
[85] J. Penfold, D. S. Sivia, E. Staples, I. Tucker, and R. K. Thomas, Langmuir **20**, 2265 (2004).
[86] J. Pan, F. A. Heberle, S. Tristram-Nagle, M. Szymanski, M. Koepfinger, J. Katsaras, and N. Kučerkae, BBA-Biomembrane **1818**, 2135 (2012).